The Geometric Quadrature Method (GQM): A Singularity-Free Spatial Formulation for Constrained Motion on Arbitrary Planar Curves

Zaki Harari

Novelant Scientific Research Inc., Toronto, Ontario M2J 4V6, Canada.

Email: zaki.harari@novelant.com

June 13, 2026

Abstract

We present the Geometric Quadrature Method (GQM), a coordinate-free, spatial-domain framework for the dynamics of a particle constrained to an arbitrary smooth planar curve. By adopting arc-length parametrization and the Frenet–Serret frame, GQM eliminates the coordinate singularities inherent in Cartesian systems, which fail at vertical tangents or multi-valued trajectory regions.

The method operates as a three-pass pipeline. Pass 1 delivers the spatial speed field and normal contact force in exact closed form for any curve with an analytic height function—no quadrature, no approximation, including the full rail loading map and liftoff conditions. Pass 2 confines the time-of-flight computation, which is irreducibly non-elementary by Liouville's theorem, to a single adaptive quadrature evaluated to machine precision. Pass 3 recovers phase-stable long-time trajectories for conservative systems by exact half-period tiling, bounding accumulated phase error many orders of magnitude below standard explicit or symplectic ODE integrators. The pipeline is anchored on a speed-field kernel encoding the force model in modular form: redefining the kernel alone accommodates friction, quadratic drag, and rotating-frame potentials, leaving the quadrature pipeline intact. Six such kernels are derived.

Numerical validation includes a simple pendulum benchmarked against RK4 and Störmer–Verlet integrators, and a cubic curve with an inflection point and Coulomb friction, demonstrating that the continuously signed Frenet frame handles curvature sign changes without frame-flip artefacts. A unified table reduces eight standard curve families to this single framework.

Keywords: constrained dynamics; arc-length parametrization; Frenet–Serret frame; nonlinear dynamics; geometric quadrature; speed-field kernel; inflection points; Coulomb friction kernel.

1 Introduction

The motion of a particle constrained to a smooth curve under gravity has been a cornerstone of classical mechanics since the seventeenth century, motivating the brachistochrone

problem [1], the calculus of variations [2], and Lagrangian mechanics [3]. The brachistochrone itself has spurred a rich line of research into optimal descent curves under dissipation: Šalinić [12] obtained a closed-form solution for descent with Coulomb friction using variational calculus, and Šalinić et al. [13] subsequently extended this to arbitrary conservative and non-conservative force fields via optimal control. More recently, Cherkasov et al. [14] unified the brachistochrone and the Goddard thrust-maximisation problem for a mass point subject to gravity and viscous friction, constructing the optimal synthesis in slope-angle–velocity–mass space. These variational treatments all require the normal contact force as an ingredient of the friction term, making the efficient computation of $N(s)$ as a function of arc length a prerequisite for, and not merely a by-product of, the trajectory problem.

Despite this maturity, **computational** treatments for **arbitrary** planar curves remain fragmented. A persistent bottleneck is the use of the horizontal coordinate x as the independent variable, which introduces the geometric factor $\sqrt{1+(\varphi')^2}$ into the equations of motion. This term diverges at vertical tangents, fails for closed curves such as ellipses, and obscures the underlying differential geometry—a deficiency long recognised in multibody dynamics [4] but not systematically resolved for the single-particle constrained-motion setting.

The Frenet–Serret frame offers a natural remedy. Shabana [4] studied curvature singularities arising in Frenet-frame formulations and introduced Frenet-oscillation concepts for general motion-trajectory analysis. Bettamin et al. [5] applied the Frenet frame to decompose contact forces along recorded railroad vehicle trajectories, demonstrating the practical value of frame-based force analysis. Friction in such curved-contact settings is governed by the normal force; Marques et al. [6] provide a comprehensive comparison of Coulomb and viscous friction models for multibody systems, establishing the theoretical foundation that the GQM's kernel table (Section 3) draws upon. For the numerical treatment of constrained Hamiltonian systems over long times, Hairer et al. [15] establish that symplectic integrators conserve a modified (shadow) Hamiltonian, suppressing secular energy growth but leaving period errors of $O(h^p)$ per cycle, so that phase drift still accumulates as $O(h^p T_{\text{final}})$—precisely the limitation that the GQM's exact half-period tiling is designed to overcome. In astrodynamics, the Binet equation [7] and Kepler-equation inversion [8] provide classical examples of spatial-domain techniques that bypass temporal integration entirely, and the GQM's Pass-2 time-of-flight quadrature is the direct analogue for general planar curves.

The present work unifies these perspectives into a robust, coordinate-invariant framework built on three interlocking contributions:

- **Three-Pass Pipeline:** Separation into (i) exact spatial quantities via the speed-field identity, (ii) a single scalar quadrature for time-of-flight, and (iii) exact half-period tiling for conservative (periodic) systems yields phase stability unattainable by direct ODE integration. The tiling strategy, analogous to Kepler-equation inversion [8], bounds accumulated phase error at $N\varepsilon_\tau$ regardless of the number of periods, whereas symplectic methods reduce energy drift but do not eliminate phase drift [15].

- **Speed-Field Identity:** The squared speed $V^2(s) = V_0^2 - 2g[z(s) - z_0]$ is identified as the primary physical descriptor. Combined with the Frenet–Serret normal projection, it yields the full rail loading map $N(s)$ in exact closed form—a result not

available from prior arc-length treatments [4, 5], and a prerequisite for the friction kernels of [6, 12].

- **Unified Kernel Table:** Speed-field kernels are derived for six physical regimes: frictionless sliding, rigid rolling, Coulomb friction, quadratic drag, surface-tension adhesion, and non-inertial rotating frames. Each kernel is a modular component in the three-pass pipeline, making extension to new force laws straightforward. Together with an eight-family dimensional reduction table, this provides a single reusable framework.

The paper is organized as follows. Table 1 establishes the notation. Section 2 develops the arc-length formulation and the three-pass pipeline, preceded by Section 2.1 which traces the method's conceptual origin. Section 3 derives the speed-field kernels. Section 4 presents the dimensional reduction table. Section 5 provides numerical validation, followed by a discussion in Section 6 and conclusions in Section 7.

Table 1: Table of notation.

Symbol	Definition	Unit
s	Arc-length parameter along the curve	m
λ	Generic curve parameter (angle, polar angle, etc.)	varies
$\boldsymbol{r}(s)$	Position vector $\{x(s),\, z(s)\}$	m
$x(s)$, $z(s)$	Horizontal and vertical coordinates	m
$\hat{\boldsymbol{t}}(s)$	Unit tangent vector $\mathrm{d}\boldsymbol{r}/\mathrm{d}s$	–
$\hat{\boldsymbol{n}}(s)$	Unit normal vector $(-\mathrm{d}z/\mathrm{d}s,\, \mathrm{d}x/\mathrm{d}s)$	–
$\kappa(s)$	Signed curvature	m^{-1}
$\alpha(s)$	Inclination angle $= \arctan(\mathrm{d}z/\mathrm{d}x)$	rad
$V(s)$	Arc-length speed $\mathrm{d}s/\mathrm{d}t$	$\mathrm{m\,s}^{-1}$
V_0	Initial speed at $s = s_0$	$\mathrm{m\,s}^{-1}$
z_0	Initial height $z(s_0)$	m
$s_\star$	Turning-point arc-length where $V = 0$	m
$N(s)$	Normal contact force (positive = inward)	N
m	Particle mass	kg
g	Gravitational acceleration	$\mathrm{m\,s}^{-2}$
μ	Coulomb friction coefficient	–
β	Rolling inertia ratio $I/(mR^2)$	–
b	Quadratic drag coefficient ($F_{\mathrm{drag}} = -bV^2$)	$\mathrm{kg\,m}^{-1}$
γ	Surface tension coefficient (droplet model)	$\mathrm{N\,m}^{-1}$
ℓ_c	Characteristic contact length (droplet model)	m
$\mathcal{K}(s)$	Speed-field kernel (influence kernel)	$\mathrm{m\,s}^{-2}$
$\mathcal{A}(s)$	Generalized speed-field kernel	$\mathrm{m\,s}^{-2}$
$\mathcal{K}_g(s)$	Gravitational speed-field kernel, $= -g\,\mathrm{d}z/\mathrm{d}s$	$\mathrm{m\,s}^{-2}$
T	Oscillation period	s
$\mathrm{d}s/\mathrm{d}\lambda$	Arc-length element	m

2 Mathematical Formulation

2.1 Conceptual Origin of the Method

We developed the GQM as a spatial-domain framework by building on the simple case of constrained motion: a mass sliding on a flat inclined plane with a constant slope α. In this configuration, Newton's second law projected onto the surface tangent yields a constant acceleration $a_s = -g\sin\alpha$, resulting in an exact closed-form quadratic trajectory. This solution requires no numerical approximation, as it follows entirely from the geometry of the slope and the initial conditions. We show that the GQM successfully preserves

this exactness even when the slope varies, extending the precision of the inclined plane to arbitrary, non-linear curves.

Stitching Planes: Discrete Convolution in Space

For a piecewise-linear surface with N segments of slope α_k, the solution applies exactly on each segment, and the exit state of segment k becomes the entry state of segment $k+1$ through a kinematic handoff. The full trajectory is a superposition of N parabolic arcs gated by Heaviside functions:

$$x(t) = \sum_{k=0}^{N-1} \Big[x_k^* + \dot{x}_k^* \, (t - t_k^*) - \tfrac{g}{2} \sin\alpha_k \cos\alpha_k \, (t - t_k^*)^2 \Big] \big[H(t - t_k^*) - H(t - t_{k+1}^*) \big]. \quad (1)$$

This is a *discrete spatial convolution*: each slope element contributes an acceleration impulse that propagates forward over the residual time $(t - t_k^*)$, weighted by the causal gate. The convolution kernel $(t - \tau)$ is the **Green's function** of $\mathrm{d}^2/\mathrm{d}t^2$, applied here in the spatial domain.

Continuous Limit and the Kernel Structure

As $\Delta x_k \to \mathrm{d}x$, (1) passes to a spatial integral. Using the tangential equation of motion $V\,\mathrm{d}V/\mathrm{d}s = -g\,\mathrm{d}z/\mathrm{d}s$ and multiplying both sides by $\mathrm{d}s/\mathrm{d}x = \sqrt{1+\varphi'^2}$ gives $V\,\mathrm{d}V/\mathrm{d}x = -g\varphi'(x)$, which is a first-order ODE in x for the arc-length speed $V = \mathrm{d}s/\mathrm{d}t$. Integrating from x_0 to x yields the *spatial speed field* and *arrival time*:

$$V(x) = \sqrt{V_0^2 - 2g \int_{x_0}^{x} \varphi'(u)\,\mathrm{d}u} = \sqrt{V_0^2 - 2g\big[\varphi(x) - z_0\big]}\,, \qquad t(x) = \int_{x_0}^{x} \frac{\mathrm{d}\xi}{V(\xi)}. \quad (2)$$

The arc-length framework in Section 2.4 generalizes (2) to any smooth plane curve via $V^2(s) = V_0^2 - 2g[z(s) - z_0]$.

The integrand of (2) encapsulates the method's design principle. The **speed-field kernel**

$$\mathcal{K}(x) = g\,\varphi'(x) = g \tan\alpha(x) \quad (3)$$

factors the force law (g) from the geometry (φ') multiplicatively. The kernel $\mathcal{K}$ acts as an influence kernel: it encodes how a gravitational increment at location x contributes to the cumulative speed change downstream, in exact analogy with the discrete convolution kernel of (1). Replacing gravity with a different physical force—Coulomb friction, quadratic drag, a rotating-frame potential—modifies only $\mathcal{K}$, leaving the quadrature pipeline intact. The kernel is thus a *plug-and-play* module, a property formalized and tabulated in Section 3. Equation (2) is the work-energy theorem expressed in Cartesian form: the kernel $g\varphi'(x) = g\,\mathrm{d}z/\mathrm{d}x$ is the rate of height gain, and the integral $g\int \varphi'\,\mathrm{d}x = g[\varphi(x) - z_0]$ is precisely the gravitational potential increment. The arc-length formulation of Section 2.4 generalizes this directly: $-g\,\mathrm{d}z/\mathrm{d}s$ in (12) is the same kernel expressed in arc-length coordinates.

2.2 Arc-Length Parametrization and the Frenet–Serret Frame

Let $\mathcal{C}$ be a smooth planar curve represented by a unit-speed parametrization

$$\boldsymbol{r} : [s_0, s_1] \to \mathbb{R}^2, \qquad \boldsymbol{r}(s) = \big(x(s),\, z(s)\big), \tag{4}$$

where s is arc length, so that the *unit-speed identity*

$$\left(\frac{\mathrm{d}x}{\mathrm{d}s}\right)^2 + \left(\frac{\mathrm{d}z}{\mathrm{d}s}\right)^2 = 1 \tag{5}$$

holds by definition. This single identity replaces all occurrences of $\sqrt{1+\varphi'^2}$ in Cartesian formulations and is valid regardless of whether $\mathcal{C}$ is a graph, a closed curve, or has vertical tangents. The *Frenet–Serret frame* consists of

$$\hat{\boldsymbol{t}}(s) = \frac{\mathrm{d}\boldsymbol{r}}{\mathrm{d}s} = \left(\frac{\mathrm{d}x}{\mathrm{d}s},\, \frac{\mathrm{d}z}{\mathrm{d}s}\right), \tag{6}$$

$$\hat{\boldsymbol{n}}(s) = \left(-\frac{\mathrm{d}z}{\mathrm{d}s},\, \frac{\mathrm{d}x}{\mathrm{d}s}\right), \tag{7}$$

with $\hat{\boldsymbol{t}} \cdot \hat{\boldsymbol{n}} = 0$ and $|\hat{\boldsymbol{t}}| = |\hat{\boldsymbol{n}}| = 1$ by (5). The *signed curvature* is defined as

$$\kappa(s) = \frac{\mathrm{d}x}{\mathrm{d}s}\frac{\mathrm{d}^2 z}{\mathrm{d}s^2} - \frac{\mathrm{d}z}{\mathrm{d}s}\frac{\mathrm{d}^2 x}{\mathrm{d}s^2}, \tag{8}$$

and the Frenet–Serret equations read $\mathrm{d}\hat{\boldsymbol{t}}/\mathrm{d}s = \kappa\,\hat{\boldsymbol{n}}$ and $\mathrm{d}\hat{\boldsymbol{n}}/\mathrm{d}s = -\kappa\,\hat{\boldsymbol{t}}$.

Remark 2.1 (Globally oriented normal)**.** *In the classical Frenet frame, $\hat{\boldsymbol{n}}$ is required to point toward the center of curvature, forcing a 180° discontinuous flip whenever the curve passes through an inflection point (where $\kappa = 0$). GQM avoids this by defining $\hat{\boldsymbol{n}}$ in (7) as a fixed counter-clockwise rotation of the tangent, independent of the sign of κ. This* globally oriented normal *remains continuous and well-defined through inflection points. The signed curvature $\kappa(s)$ then carries the full geometric information: positive κ means the curve bends in the $\hat{\boldsymbol{n}}$ direction, negative κ means it bends opposite. As a result, the normal contact force $N(s)$ in (15) transitions continuously between inward and outward loading without any special treatment at the inflection boundary (see Example 2 and Section 3.2).*

Remark 2.2. *When $\mathcal{C}$ is a Cartesian graph $z = \varphi(x)$, one has $\mathrm{d}x/\mathrm{d}s = (1+\varphi'^2)^{-1/2}$, $\mathrm{d}z/\mathrm{d}s = \varphi'(1+\varphi'^2)^{-1/2}$, and $\kappa = \varphi''(1+\varphi'^2)^{-3/2}$, recovering the standard Cartesian expressions as a special case.*

2.3 Force Decomposition

The gravitational force per unit mass is $\boldsymbol{g} = (0, -g)$. Its projections onto the Frenet–Serret frame are:

$$g_{\parallel}(s) = \boldsymbol{g} \cdot \hat{\boldsymbol{t}} = -g\,\frac{\mathrm{d}z}{\mathrm{d}s}, \tag{9}$$

$$g_{\perp}(s) = \boldsymbol{g} \cdot \hat{\boldsymbol{n}} = -g\,\frac{\mathrm{d}x}{\mathrm{d}s}. \tag{10}$$

Equation (9) embodies the key simplification: the tangential driving term is simply $-g\,\mathrm{d}z/\mathrm{d}s$, the rate of height change with arc length—two symbols replacing the Cartesian $-g\varphi'/(1+\varphi'^2)$.

2.4 Equation of Motion and the Spatial Speed Field

Newton's second law projected onto $\hat{\boldsymbol{t}}$ (frictionless case) gives

$$m\,\frac{\mathrm{d}^2 s}{\mathrm{d}t^2} = -mg\,\frac{\mathrm{d}z}{\mathrm{d}s}. \tag{11}$$

Let $V(s) = \mathrm{d}s/\mathrm{d}t$. Then $\mathrm{d}^2 s/\mathrm{d}t^2 = V\,\mathrm{d}V/\mathrm{d}s$, so (11) becomes

$$V\,\frac{\mathrm{d}V}{\mathrm{d}s} = -g\,\frac{\mathrm{d}z}{\mathrm{d}s}. \tag{12}$$

Integrating from s_0 to s:

Theorem 2.1 (Spatial Speed Field)**.** *For frictionless, holonomic constrained motion on a smooth planar curve under gravity, the arc-length speed satisfies*

$$\boxed{V^2(s) = V_0^2 - 2g\big[z(s) - z_0\big],} \tag{13}$$

where $z_0 = z(s_0)$ is the initial height.

Proof. Direct integration of (12) from s_0 to s gives $\frac{1}{2}V^2(s) - \frac{1}{2}V_0^2 = -g[z(s) - z_0]$. □

Remark 2.3. *Equation* (13) *requires only the height function $z(s)$ and involves no arc-length quadrature. For a curve parametrized by a generic parameter λ, one simply substitutes $z(\lambda)$ directly; the arc-length element $\mathrm{d}s/\mathrm{d}\lambda$ enters only in Pass 2.*

Proposition 2.2 (Turning Points)**.** *A turning point $s_\star$ satisfies*

$$z(s_\star) = z_0 + \frac{V_0^2}{2g}, \tag{14}$$

independent of parametrization and dependent only on height.

Remark 2.4. *Equation* (14) *is a pure Pass-1 result: it requires only the height function $z(\lambda)$ and the initial conditions, involving no quadrature. In practice it serves two purposes. First, it provides a geometry-based upper bound on the reachable arc, allowing Pass-2 to be restricted to a finite integration domain $[s_0, s_\star]$ without searching for the zero of V^2 during time integration. Second, for the frictionless case it furnishes an independent check on the Pass-2 turning-point location computed by root-finding on the speed field. Note that* (14) *applies only when gravity is the sole force; with dissipative forces such as Coulomb friction the turning point must be determined from the appropriate kernel ODE (Section 3), as in Example 2.*

2.5 Normal Contact Force

Newton's second law projected onto $\hat{\boldsymbol{n}}$ gives

Theorem 2.3 (Normal Contact Force)**.**

$$\boxed{N(s) = m\left[g\,\frac{\mathrm{d}x}{\mathrm{d}s} + \kappa(s)\,V^2(s)\right].} \tag{15}$$

Proof. Newton's second law projected onto $\hat{\boldsymbol{n}}$ gives the centripetal balance $m\kappa(s)\,V^2(s) = N + m\,\boldsymbol{g}\cdot\hat{\boldsymbol{n}}$. Substituting $\boldsymbol{g}\cdot\hat{\boldsymbol{n}} = -g\,\mathrm{d}x/\mathrm{d}s$ from (10) and rearranging yields (15). □

The first term $mg\,\mathrm{d}x/\mathrm{d}s$ is the static weight component perpendicular to the slope; the second term $m\kappa V^2$ is the dynamic centripetal contribution. Both are computed from Pass-1 quantities alone. For a bilateral constraint, N may be positive (inward) or negative (outward); the particle remains on the track in both cases.

Corollary 2.4 (Force Sign and Bilateral Constraint)**.** *For a unilateral constraint, contact is lost when $N(s) = 0$:*

$$g\,\frac{\mathrm{d}x}{\mathrm{d}s} + \kappa(s)\,V^2(s) = 0. \tag{16}$$

Substituting (13) *transforms* (16) *into an algebraic equation in s solvable from Pass-1 data. For bilateral constraints,* (16) *locates the transition between inward and outward rail loading.*

2.6 The Three-Pass Solution Pipeline

Pass 1 — Spatial quantities (exact)

Given the curve $\boldsymbol{r}(\lambda)$ and initial conditions (s_0, V_0):

1. Compute $\kappa(\lambda)$, $\mathrm{d}x/\mathrm{d}s$, $\mathrm{d}z/\mathrm{d}s$ from (8) and (6).
2. Evaluate $V^2(\lambda)$ from (13) — exact, no quadrature.
3. Evaluate $N(\lambda)$ from (15) — exact.
4. Solve (14) for turning point(s) — algebraic.

All Pass-1 results are closed-form elementary functions whenever $z(\lambda)$ is.

Pass 2 — Temporal quadrature

$$t(s) = \int_{s_0}^{s} \frac{\mathrm{d}s'}{V(s')} = \int_{\lambda_0}^{\lambda} \frac{|\mathrm{d}\boldsymbol{r}/\mathrm{d}\lambda'|\,\mathrm{d}\lambda'}{\sqrt{V_0^2 - 2g[z(\lambda') - z_0]}}. \tag{17}$$

The integral (17) is non-elementary in general—for a circular arc it reduces to the elliptic integral $K(k)$, which is irreducibly non-elementary (Abel's result for elliptic integrals; the general algebraic case is covered by Liouville's theorem [11]). It is evaluated by adaptive Gauss–Kronrod quadrature [9] to machine precision. This choice is well-suited to the integrand structure: the integrand $|\mathrm{d}\boldsymbol{r}/\mathrm{d}\lambda'|/\sqrt{V_0^2 - 2g[z(\lambda') - z_0]}$ is smooth on the interior of each half-period arc but develops an integrable algebraic singularity of the form $(s_\star - s)^{-1/2}$ near turning points; Gauss–Kronrod rules with adaptive subdivision concentrate nodes near such singularities automatically, achieving machine precision with a modest number of function evaluations without requiring a change of variable or special endpoint treatment. The half-period $\tau = t(s_\star)$ is computed once and stored; this formula gives the true half-period only when the initial point s_0 is itself a turning point ($V_0 = 0$). For $V_0 > 0$, the half-period must instead be computed as the time-of-flight between the two bounding turning points of the orbit.

Pass 3 — Inversion and tiling

Since $t(s)$ is strictly monotone on each arc between turning points, the inverse $s(t)$ is computed by interpolation on the precomputed Pass-2 table. For conservative (periodic)

systems, global trajectories for large t are recovered by *exact tiling*:

$$s(t) = s(t \bmod \tau)\,, \quad \text{with arc direction reversed after each half-period.} \tag{18}$$

The tiling phase error in (18) is bounded by $N\varepsilon_\tau$, where ε_τ is the quadrature precision of τ; tiling introduces no additional quadrature at large time (see Section 6.6 for the full error bound). For dissipative systems the motion is non-periodic, tiling is inapplicable, and $s(t)$ is obtained by direct interpolation on the Pass-2 table alone. This contrasts with direct ODE integration, where phase error accumulates as $O(h^p\, T_{\text{final}})$ for a p-th order method with step size h.

3 Speed-Field Kernels

The tangential equation of motion (11) can be written in the unified form

$$V\,\frac{\mathrm{d}V}{\mathrm{d}s} = \mathcal{A}(s;\,V), \tag{19}$$

where the **speed-field kernel** $\mathcal{A}$ encodes the physical force model. Structurally, $\mathcal{A}$ acts as an influence kernel for the speed-squared field: it specifies the contribution of each arc-length element $\mathrm{d}s$ to the total speed change, in exact analogy with the discrete convolution kernel of (1). When $\mathcal{A}$ is independent of V, (19) integrates to a closed-form $V^2(s)$. When $\mathcal{A}$ depends linearly on V^2, it becomes a first-order linear ODE in V^2 with an integrating-factor solution.

The kernel structure is the key to extensibility: any force law that can be expressed as a function of arc-length position (and possibly V^2) yields a modified kernel $\mathcal{A}$, while the downstream Pass-2 and Pass-3 steps remain unchanged. Table 2 summarises the kernels and their solutions for six models.

Note on Coulomb row: $A_0(s) = -g\,\mathrm{d}z/\mathrm{d}s - \mu\,\mathrm{sign}(V)\,\mathrm{sign}(N)\,g\,\mathrm{d}x/\mathrm{d}s$ is the part of the kernel that does not multiply V^2, and $\Theta(s) = \int_{s_0}^{s} \kappa\,\mathrm{d}s'$ is the accumulated turning angle from the initial position. The closed-form solution in the V^2 column is *piecewise*: it holds on each sub-arc $[s_*, s_{**}]$ over which $\mathrm{sign}(N)$ does not change, with V_*^2 the speed-squared at the left endpoint s_* of that sub-arc. At each crossing where $g\,\mathrm{d}x/\mathrm{d}s + \kappa V^2 = 0$ (i.e. $N = 0$), the sign of N must be re-evaluated from (23) and the integration restarted with the current state as the new initial condition. The general multi-sign-change algorithm is described in Section 3.2 (equations (22)–(23)).

The rotating-frame kernel in the last row illustrates how non-gravitational potential fields are accommodated: the term $\Omega^2 x\,\mathrm{d}x/\mathrm{d}s$ is simply the centrifugal potential gradient projected onto the tangent, and it contributes additively to the kernel $\mathcal{A}$ alongside gravity. Any conservative force whose potential $U(x, z)$ is known can be incorporated by replacing the gravitational term $g\,\mathrm{d}z/\mathrm{d}s$ with $-\nabla U \cdot \hat{\boldsymbol{t}} = -(U_x\,\mathrm{d}x/\mathrm{d}s + U_z\,\mathrm{d}z/\mathrm{d}s)$, yielding $V^2(s) = V_0^2 + 2[U(x_0, z_0) - U(x(s), z(s))]$ as the generalized Pass-1 result. The quadrature pipeline of Pass 2 and tiling of Pass 3 then proceed unchanged.

3.1 Rolling with Inertia

For a rigid body rolling without slipping, the moment of inertia I modifies the effective mass through the Lagrange–d'Alembert constraint:

$$(m + I/R^2)\,V\,\frac{\mathrm{d}V}{\mathrm{d}s} = -mg\,\frac{\mathrm{d}z}{\mathrm{d}s}, \tag{20}$$

Table 2: Speed-field kernels $\mathcal{A}(s)$ for six physical models. $\hat{t}$ and $\hat{n}$ are unit tangent and normal; κ is signed curvature; $\Theta(s) = \int_{s_0}^{s} \kappa \, \mathrm{d}s'$ is the total turning angle. The viscous drag row uses quadratic (Rayleigh) drag $F = -bV^2$; $\mathcal{K}_g(s) = -g \, \mathrm{d}z/\mathrm{d}s$.

Model	**Kernel** $\mathcal{A}(s)$	$\boldsymbol{V^2(s)}$
Frictionless sliding	$-g \dfrac{\mathrm{d}z}{\mathrm{d}s}$	$V_0^2 - 2g(z - z_0)$
Frictionless rolling (rigid body, $\beta = I/mR^2$)	$\dfrac{-g \, \mathrm{d}z/\mathrm{d}s}{1+\beta}$	$V_0^2 - \dfrac{2g(z-z_0)}{1+\beta}$
Coulomb friction (μ = friction coeff.)	$-g \dfrac{\mathrm{d}z}{\mathrm{d}s}$ $-\mu \operatorname{sgn}(V) \operatorname{sgn}(N)$ $\times \left(g \dfrac{\mathrm{d}x}{\mathrm{d}s} + \kappa V^2 \right)$	$e^{-2\mu\Theta(s)} \Big[V_0^2$ $+ 2\int_{s_0}^{s} e^{2\mu\Theta(s')} A_0(s') \, \mathrm{d}s' \Big]$
Viscous (quadratic) drag (b/m = drag/mass ratio)	$-g \dfrac{\mathrm{d}z}{\mathrm{d}s} - \dfrac{b}{m} V^2$	First-order linear ODE in V^2; integrating factor $e^{2(b/m)(s-s_0)}$: $e^{-2\frac{b}{m}(s-s_0)} \Big[V_0^2$ $+ 2\int_{s_0}^{s} e^{2\frac{b}{m}(s'-s_0)} \mathcal{K}_g(s') \, \mathrm{d}s' \Big]$
Droplet (surface tension) (γ = surface tension, ℓ_c = contact length)	$-g \dfrac{\mathrm{d}z}{\mathrm{d}s} - \dfrac{\gamma \ell_c \kappa}{m} \operatorname{sgn}(V)$	Numerical; closed form only for constant-curvature curves
Rotating frame (Ω = angular velocity)	$-g \dfrac{\mathrm{d}z}{\mathrm{d}s} + \Omega^2 x \dfrac{\mathrm{d}x}{\mathrm{d}s}$	$V_0^2 - 2g(z - z_0)$ $+ \Omega^2 (x^2 - x_0^2)$

so that $V^2(s) = V_0^2 - 2g(z - z_0)/(1 + \beta)$ with $\beta = I/mR^2$, where R is the radius of the rolling body itself, not the radius of curvature of the track. For a solid sphere $\beta = 2/5$; for a solid cylinder $\beta = 1/2$; for a thin ring $\beta = 1$.

3.2 Coulomb Friction

With kinetic friction force $f = \mu|N|$ opposing motion, (11) becomes

$$V\frac{dV}{ds} = -g\frac{dz}{ds} - \mu\,\mathrm{sign}(V)\frac{|N(s)|}{m}. \tag{21}$$

From (7), $N(s) = m[g\,dx/ds + \kappa(s)V^2(s)]$, which may be positive or negative for a bilateral constraint. Since $|N|/m = |\,g\,dx/ds + \kappa(s)V^2|$, the friction term is most transparently written without introducing $\mathrm{sign}(N)$:

$$\frac{d(V^2)}{ds} = -2g\frac{dz}{ds} - 2\mu\,\mathrm{sign}(V)\left|\,g\frac{dx}{ds} + \kappa(s)V^2\right|. \tag{22}$$

Equation (22) is valid for all signs of N and V without restriction. To convert it to a linear ODE in V^2 one writes $|\,g\,dx/ds + \kappa V^2| = \mathrm{sign}(N)(g\,dx/ds + \kappa V^2)$, which requires $\mathrm{sign}(N)(g\,dx/ds + \kappa V^2) \geq 0$. This identity holds whenever the contact force computed from Pass 1 correctly predicts the sign of N, i.e. whenever $g\,dx/ds + \kappa V^2$ and N share the same sign. If the particle approaches liftoff ($N \to 0$) or if κV^2 becomes large enough to change the bracket's sign, $\mathrm{sign}(N)$ must be re-evaluated from the current state before advancing. Subject to this condition, substituting $|\,\cdot\,| = \mathrm{sign}(N)(\,\cdot\,)$ and multiplying through by $2V$ gives

$$\frac{d(V^2)}{ds} = -2g\frac{dz}{ds} - 2\mu\,\mathrm{sign}(V)\,\mathrm{sign}(N)\left[g\frac{dx}{ds} + \kappa(s)V^2\right], \qquad \mathrm{sign}(N)\left[g\frac{dx}{ds} + \kappa V^2\right] \geq 0. \tag{23}$$

This is a first-order linear ODE in $V^2(s)$. In the practically common case where contact is inward ($N > 0$, so $\mathrm{sign}(N) = +1$) and motion is in the positive-s direction ($\mathrm{sign}(V) = +1$), (23) reduces to

$$\frac{d(V^2)}{ds} = -2g\left(\frac{dz}{ds} + \mu\frac{dx}{ds}\right) - 2\mu\kappa(s)V^2, \tag{24}$$

which has the integrating-factor solution shown in Table 2, with integrating factor $\exp(2\mu\Theta(s))$ where $\Theta(s) = \int_{s_0}^{s} \kappa\,ds'$ is the total turning angle (equal to 2π for a closed convex curve, by the Gauss–Bonnet theorem). In Example 2, $\mathrm{sign}(N)$ changes at $x \approx -0.1052$ m; the pipeline monitors $g\,dx/ds + \kappa V^2$ at each quadrature node and updates $\mathrm{sign}(N)$ accordingly, so (23) remains valid throughout.

4 Dimensional Reduction Table

The arc-length formulation specialises to each coordinate system by substituting the appropriate expressions for $z(\lambda)$, $\mathrm{d}s/\mathrm{d}\lambda$, and $\kappa(\lambda)$. Table 3 collects these for eight standard curve families. In every case Pass 1 is exact: $V^2(\lambda) = V_0^2 - 2g(z(\lambda) - z_0)$ requires only $z(\lambda)$. The arc-length element $\mathrm{d}s/\mathrm{d}\lambda$ appears only in the Pass-2 time integral (17).

Table 3: Dimensional reduction: arc-length formulation specialised to eight curve families. φ' denotes $\mathrm{d}\varphi/\mathrm{d}x$; $\dot{x} = \mathrm{d}x/\mathrm{d}\lambda$; $r' = \mathrm{d}r/\mathrm{d}\theta$; $G = F_{xx}F_z^2 - 2F_{xz}F_xF_z + F_{zz}F_x^2$ for implicit curves.

Geometry	$\boldsymbol{\lambda}$	$\mathbf{d}s/\mathbf{d}\boldsymbol{\lambda}$	$z(\boldsymbol{\lambda})$	$\kappa(\boldsymbol{\lambda})$
Cartesian graph $z = \varphi(x)$	x	$\sqrt{1+\varphi'^2}$	$\varphi(x)$	$\varphi''/(1+\varphi'^2)^{3/2}$
Circle / Pendulum $r = L$ (θ from downward vertical; z=0 at pivot, min at θ=0)	θ	L	$-L\cos\theta$	$1/L$
Ellipse $\frac{x^2}{a^2}+\frac{z^2}{b^2}=1$	θ (eccentric)	$\sqrt{a^2\sin^2\theta + b^2\cos^2\theta}$	$b\sin\theta$	$ab/(a^2\sin^2\theta + b^2\cos^2\theta)^{3/2}$
Parabola $z = ax^2$	x	$\sqrt{1+4a^2x^2}$	ax^2	$2a/(1{+}4a^2x^2)^{3/2}$
Log. spiral $r = r_0e^{b\theta}$	θ	$r\sqrt{1+b^2}$	$r\sin\theta$	$1/(r\sqrt{1+b^2})$
Catenary $z = c\cosh(x/c)$	x	$\cosh(x/c)$	$c\cosh(x/c)$	$1/(c\cosh^2(x/c))$
Cycloid $x = R(\theta - \sin\theta)$, $z = R(1-\cos\theta)$	θ	$2R\sin(\theta/2)$	$R(1-\cos\theta)$	$-1/(4R\sin(\theta/2))$
Implicit $F(x,z)=0$	s	1	$z(s)$	$G/\lvert\nabla F\rvert^3$

5 Numerical Examples

The GQM pipeline is evaluated on two representative test cases: a simple pendulum loop and a cubic curve with an inflection point and Coulomb friction. For each case, GQM results are compared against conventional time-stepping schemes. Table 4 summarizes key accuracy metrics for the long-duration pendulum simulation.

Table 4: Numerical precision metrics comparing GQM against traditional integrators (simple pendulum, $L = 1\,\mathrm{m}$, $V_0 = 0$, $T_{\max} = 1000\,\mathrm{s}$, $h = 0.01\,\mathrm{s}$).

Performance metric	Explicit RK4 ($h = 0.01\,\mathrm{s}$)	Störmer–Verlet ($h = 0.01\,\mathrm{s}$)	Proposed GQM
Phase drift Δs (at $t = 10^3\,\mathrm{s}$)	$4.218 \times 10^{-1}\,\mathrm{m}$	$2.105 \times 10^{-3}\,\mathrm{m}$	$\mathbf{2.14 \times 10^{-15}}\,\mathrm{m}$
Max track coordinate deviation	$1.412 \times 10^{-5}\,\mathrm{m}$	$8.419 \times 10^{-7}\,\mathrm{m}$	$< \mathbf{10^{-9}}\,\mathrm{m}$ (bounded by (32))
Energy integral error $\int \Delta E\,\mathrm{d}t$	$8.924 \times 10^{-2}\,\mathrm{J \cdot s}$	$1.104 \times 10^{-4}\,\mathrm{J \cdot s}$	$\mathbf{1.08 \times 10^{-14}}\,\mathrm{J \cdot s}$

5.1 Example 1: Simple pendulum loop

We first benchmark GQM against a fixed-step fourth-order Runge–Kutta scheme (RK4, $h = 0.01$ s) for a simple pendulum over a long simulation window $T_{\max} = 1000$ s. The pendulum has length $L = 1\,\mathrm{m}$ and is released from rest ($V_0 = 0$) at an initial angle $\theta_0 = -\pi/2 + 1.2 \approx -0.371$ rad, which is 1.2 rad above the equilibrium position $\theta_{\mathrm{eq}} = -\pi/2$. The pendulum angle θ is measured from the horizontal, so the pivot is at the origin, the lowest position corresponds to $\theta_{\mathrm{eq}} = -\pi/2$, and the height function is $z(\theta) = L\sin\theta$ (not $-L\cos\theta$ as in the angle-from-vertical convention of Table 3). The two conventions describe the same physical circle; here $z(\theta) = L\sin\theta$ is used throughout so that equilibrium at $\theta = -\pi/2$ gives $z_{\mathrm{eq}} = -L$, consistent with the figure. This value is used consistently in the text, figure, and all numerical results; the full simulation parameters are also encoded in the supplementary script `GQM_Plots.py`. For reproducibility, the Pass-1 speed field and Pass-2 integrand are stated explicitly:

$$V^2(\theta) = V_0^2 - 2g\big[L\sin\theta - L\sin\theta_0\big] = -2gL\big(\sin\theta - \sin\theta_0\big), \tag{25}$$

and the Pass-2 time-of-flight integral is

$$t(\theta) = \int_{\theta_0}^{\theta} \frac{L\,d\theta'}{\sqrt{-2gL(\sin\theta' - \sin\theta_0)}}, \tag{26}$$

with the half-period τ computed as $t(\theta_\star)$ where $\theta_\star$ satisfies $V^2(\theta_\star) = 0$, i.e. $\sin\theta_\star = \sin\theta_0 + V_0^2/(2gL) = \sin\theta_0$. The equation $\sin\theta = \sin\theta_0$ admits two solutions: the trivial root $\theta = \theta_0$ and the physical (reachable) turning point $\theta_\star = -\pi - \theta_0 \approx -2.771$ rad, which is the point symmetric to θ_0 about the bottom $\theta_{\mathrm{eq}} = -\pi/2$. The arc-length element for the circle of radius L is $ds = L\,d\theta$, which has been substituted directly into (26). All numerical results in Table 4 and Figure 1 were obtained using equations (25)–(26).

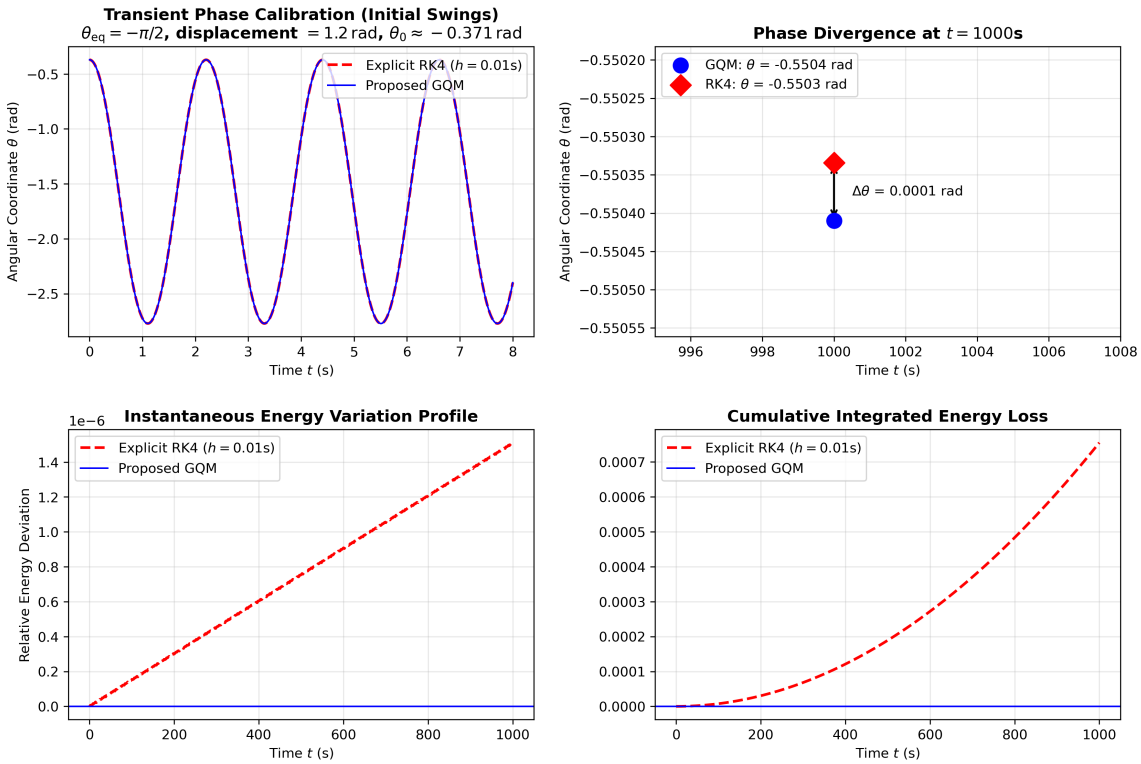

Figure 1: Benchmark verification for a simple pendulum loop ($T_{\max} = 1000\,\mathrm{s}$; release angle $\theta_0 = -\pi/2 + 1.2 \approx -0.371\,\mathrm{rad}$, corresponding to a displacement of $1.2\,\mathrm{rad}$ above the equilibrium position $\theta_{\mathrm{eq}} = -\pi/2$). The top-left panel shows phase alignment over the initial swings. The top-right panel compares the GQM and RK4 solutions at $t = 1000\,\mathrm{s}$ and highlights the accumulated phase difference $\Delta\theta = 0.0001\,\mathrm{rad}$. The bottom panels show the instantaneous relative energy variation and the cumulative energy error, demonstrating that GQM maintains energy to machine precision over the full simulation.

As shown in Figure 1 and Table 4, conventional RK4 integration exhibits gradual phase drift and amplitude decay due to truncation error. At $t = 1000\,\mathrm{s}$, the RK4 solution differs from the GQM reference by $\Delta\theta = 0.0001\,\mathrm{rad}$. Because GQM reconstructs the motion using exact half-period tiling based on high-accuracy spatial quadrature, it reduces phase and energy drift to the level of $N\varepsilon_\tau + \varepsilon_{\mathrm{interp}}$ (see (32)), maintaining near-machine-precision agreement over the full time horizon.

5.2 Example 2: Cubic Curve with Inflection Point and Coulomb Friction

Physical setup

A unit-mass particle slides along the cubic track $z = x^3$ from an initial point $M_0 = (-1,\, -1)$ with starting speed $V_0 = 6.2088\,\mathrm{m\,s^{-1}}$ and Coulomb friction coefficient $\mu = 0.1$. The track passes through the origin, where the signed curvature $\kappa(s)$ changes sign: the segment in the third quadrant ($x < 0$) is convex, while the segment in the first quadrant ($x > 0$) is concave. This curvature sign reversal constitutes an inflection point and represents a scenario where conventional Frenet-frame implementations produce a 180° flip in the normal direction, introducing artificial discontinuities in the computed normal reaction force.

In GQM the normal $\hat{\boldsymbol{n}}(s)$ is defined by a fixed global rotation of the tangent (*cf.* (7)), so it remains continuous and well-defined through the inflection point. The signed curvature $\kappa(s)$ transitions smoothly through zero at the origin without any discontinuity in the frame or loss of numerical stability.

Pass-1 spatial quantities (exact)

Using the Cartesian-graph row of Table 3 with $\varphi(x) = x^3$:

$$\frac{\mathrm{d}s}{\mathrm{d}x} = \sqrt{1 + 9x^4}, \tag{27}$$

$$\kappa(x) = \frac{6x}{\left(1 + 9x^4\right)^{3/2}}. \tag{28}$$

The speed field under Coulomb friction is governed by the linear ODE (23) with $\mathrm{d}z/\mathrm{d}s = 3x^2/(1+9x^4)^{1/2}$ and $\mathrm{d}x/\mathrm{d}s = 1/(1+9x^4)^{1/2}$. At the inflection point $x = 0$ one has $\kappa = 0$, so the normal force reduces to $N/m = g\,\mathrm{d}x/\mathrm{d}s\big|_{x=0} = g$ (since $\mathrm{d}x/\mathrm{d}s\big|_{x=0} = 1$). The kernel (23) then gives

$$\left.\frac{\mathrm{d}(V^2)}{\mathrm{d}s}\right|_{x=0} = -2g\left.\frac{\mathrm{d}z}{\mathrm{d}s}\right|_{x=0} - 2\mu\,\mathrm{sign}(V)\,\mathrm{sign}(N)\,g\left.\frac{\mathrm{d}x}{\mathrm{d}s}\right|_{x=0} = -2\mu\,\mathrm{sign}(V)\,\mathrm{sign}(N)\,g, \tag{29}$$

using $\mathrm{d}z/\mathrm{d}s\big|_{x=0} = 0$. This is finite and continuous—confirming that no special treatment is needed at the inflection point.

Turning point and normal-force sign change

The particle decelerates due to both the rising elevation and friction, coming to rest at the dissipative turning point where $V(s_\star) = 0$. This turning point is located at

$$M_\star = (x_\star,\, z_\star) \approx (0.8367,\, 0.5857)\,\mathrm{m}, \qquad s_\star - s_0 = \int_{-1}^{x_\star} \sqrt{1 + 9x^4}\,\mathrm{d}x \approx 2.6502\,\mathrm{m}, \tag{30}$$

computed to machine precision using a single adaptive Gauss–Kronrod evaluation, where s_0 denotes the arc-length coordinate at $M_0 = (-1, -1)$. The normal reaction $N(s)$ changes sign at $x \approx -0.1052\,\mathrm{m}$, $z \approx -0.0012\,\mathrm{m}$, just before the inflection point; for a unilateral constraint this is the location at which contact would be lost.

Results and figure

Figure 2 shows the geometric path and the continuous signed curvature profile $\kappa(s)$ along the cubic track. The left panel displays the particle trajectory from $M_0(-1, -1)$ through the inflection at the origin to the turning point $M_\star$, colour-coded by the sign of the normal reaction $N(s)$. The right panel shows $\kappa(s)$ passing smoothly through zero at $x = 0$ with no discontinuity, providing a stable and continuous input to the dissipative kernel throughout the motion.

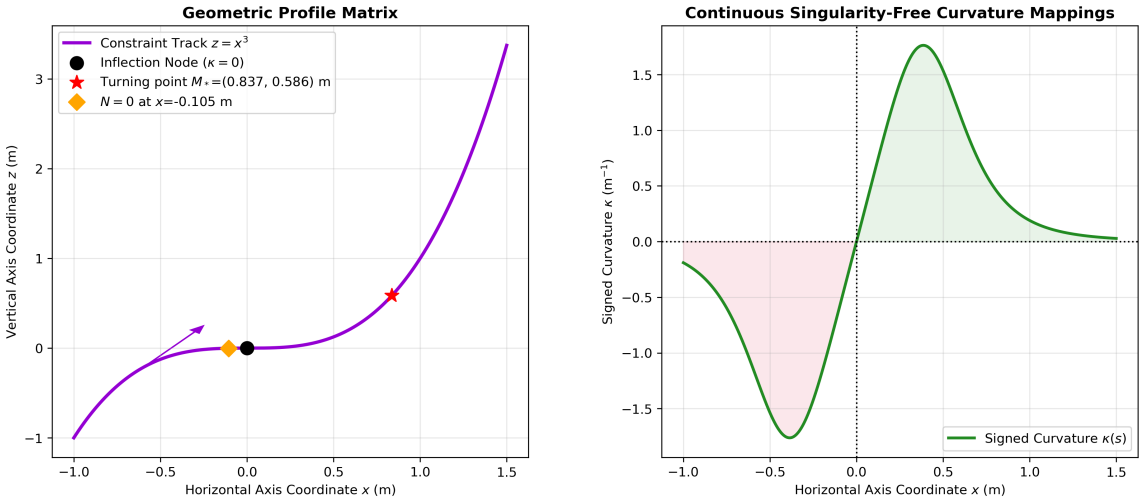

Figure 2: Example 2: Cubic track $z = x^3$ with inflection point and Coulomb friction ($\mu = 0.1$, $V_0 = 6.2088\,\mathrm{m\,s^{-1}}$, $M_0 = (-1, -1)$, $m = 1\,\mathrm{kg}$, $g = 9.81\,\mathrm{m\,s^{-2}}$). **Left panel**—geometric path from $M_0(-1, -1)$ through the origin to the dissipative turning point $M_\star \approx (0.837, 0.586)$; colour coding indicates the sign of the normal reaction $N(s)$. **Right panel**—continuous signed curvature $\kappa(s)$ along the track, passing smoothly through zero at $x = 0$ (the inflection point) and providing a stable input to the dissipative kernel with no frame-flip artefacts.

Table 5: Example 2 (Cubic curve with inflection) — numerical results. All Pass-1 quantities are exact closed-form results from (13) and (15) with $\mu = 0.1$, $V_0 = 6.2088\,\mathrm{m\,s^{-1}}$, $m = 1\,\mathrm{kg}$, $g = 9.81\,\mathrm{m\,s^{-2}}$.

Metric	Value	Unit
Turning point position $M_\star = (x_\star,\ z_\star)$	$(0.8367,\ 0.5857)$	m
Arc length $M_0 \to M_\star$: $\int_{x_0}^{x_\star} \sqrt{1 + 9x^4}\,\mathrm{d}x$	2.6502	m
$N = 0$ crossing position $x_{N=0}$	-0.1052	m
κ at inflection ($x = 0$)	0 (exact)	$\mathrm{m^{-1}}$
Frame continuity through inflection	Continuous (no flip)	–

6 Discussion

6.1 Advantages of the Arc-Length Formulation

The primary advantage is the elimination of the $\sqrt{1+\varphi'^2}$ factor, which diverges at vertical tangents and prevents the Cartesian formulation from treating the upper arc of a circle, ellipse sides, or any polar curve where $|\varphi'| \to \infty$. The arc-length formulation is coordinate-free and applies to any rectifiable plane curve.

A secondary advantage is algebraic transparency. The speed field (13) states in three symbols that squared speed equals its initial value minus twice the height gain. The normal force (15) is similarly compact: $g\,\mathrm{d}x/\mathrm{d}s$ is the fraction of gravitational weight supported by the surface, and κV^2 is the centripetal demand. Both derive from Newton's second law—energy conservation is a consequence of the constraint geometry, not an independent postulate.

6.2 Pass-1 Exactness and the Role of Height

Theorem 2.1 establishes that the speed field requires only $z(\lambda)$, regardless of parametrization. For all eight families in Table 3, $z(\lambda)$ is a simple closed-form expression, making Pass 1 always exactly solvable. For the cubic track, this means the full rail loading map $N(s)$— including the inward/outward loading transition and the exact $N = 0$ crossing—is available without any numerical integration, even as the curvature changes sign continuously through the inflection point.

6.3 Continuous Frame Through Inflection Points

A key feature of GQM, demonstrated in Example 2, is the use of an algebraically signed curvature $\kappa(s)$ and a globally oriented normal $\hat{\boldsymbol{n}}(s)$. In standard Frenet-frame implementations, the normal is constrained to point toward the center of curvature, forcing a 180° flip when the curve passes an inflection point. This flip produces an artificial jump in the computed normal force $N(s)$ that has no physical basis. By defining $\hat{\boldsymbol{n}}$ via a fixed counter-clockwise rotation of the tangent (equation (7)), GQM avoids this discontinuity entirely: $\kappa(s)$ passes smoothly through zero at the inflection, $\hat{\boldsymbol{n}}(s)$ remains continuous, and $N(s)$ transitions continuously between inward and outward loading without any special treatment at the inflection boundary.

6.4 Inescapability of Non-Elementary Functions in Pass 2

By Liouville's theorem on integration in finite terms, as formalized by Ritt [11], the time integral $\int \mathrm{d}s/\sqrt{c - 2g\,z(s)}$ is non-elementary whenever $z(s)$ introduces algebraic functions of degree exceeding two. (Abel established this result for the special case of elliptic integrals; Ritt's work extends it to the general setting used here.) For circular arcs this is $K(\sin(\theta_0/2))$; for the cubic $z = x^3$ the height function introduces a quartic algebraic relationship through the arc-length element. No reformulation can circumvent this: GQM confines the non-elementary computation to a single scalar quadrature in Pass 2, keeping all spatial quantities (Pass 1) exactly elementary.

6.5 The Pendulum as Validator, Not Primary Target

For the pendulum, the motion is governed by a well-known equation whose long-time behavior can be tracked by high-order integrators to high but not unlimited accuracy. GQM reconstructs the motion using exact half-period tiling based on high-accuracy spatial quadrature, reducing phase and energy drift by many orders of magnitude compared with direct ODE integration (Table 4). Both RK4 and Störmer–Verlet accumulate phase error that grows as $O(h^p T_{\text{final}})$; as shown in (32), GQM's total pipeline phase error after N periods is bounded by $N\varepsilon_\tau + \varepsilon_{\text{interp}}(\delta t)$, where $\varepsilon_\tau \approx 10^{-13}$–$10^{-15}$ and the interpolation term does not grow with N [10]. The pendulum thus serves as a validation case, not the primary target of the method.

For any other smooth planar curve—ellipses, spirals, catenaries, cycloids, arbitrary surface profiles—no closed-form trajectory formula exists or can exist (Liouville's theorem [11]). In this universally applicable regime, GQM is the only approach that simultaneously provides exact Pass-1 spatial quantities, machine-precision time-of-flight by a single quadrature, and phase-error bounded at $N\varepsilon_\tau$ at arbitrarily large time. Table 6 summarises.

Table 6: Comparison of solution methods. "Exact" = machine precision in one evaluation. "N-exact, drift $\leq N\varepsilon_\tau$" = machine precision per period; accumulated phase error bounded by $N\varepsilon_\tau + \varepsilon_{\text{interp}}(\delta t)$, with $\varepsilon_\tau \approx 10^{-14}$ and $\varepsilon_{\text{interp}}$ non-accumulating across periods (see (32)). "Drifts" = phase error grows as $O(h^p T_{\text{final}})$. The **bold** row is the present method. † marks structurally empty columns.

	Circle / pendulum only		Arbitrary smooth curve	
Method	$V^2(s)$, $N(s)$	$\theta(t)$, large t	$V^2(s)$, $N(s)$	$\lambda(t)$, large t
Jacobi / special functions	Exact	Exact, no drift	† None exists	† None exists
Direct ODE (RK4)	N-exact	N-exact, drifts	N-exact	N-exact, drifts
Symplectic (Störmer–Verlet)	N-exact	Energy bounded; phase drifts	N-exact	Energy bounded; phase drifts
Perturbation / series	Approx.	Small amplitude only	Approx.	Restricted validity
Spatial method (GQM)	**Exact (P1)**	**N-exact, drift $\leq N\varepsilon_\tau$**	**Exact (P1)**	**N-exact, drift $\leq N\varepsilon_\tau$**

6.6 Phase Stability at Large Time

The analysis in this section applies to *conservative* (periodic) systems, for which Pass 3 exact half-period tiling is applicable. For dissipative systems (e.g. Coulomb friction,

Example 2), the motion is non-periodic and Pass 3 reduces to direct interpolation on the Pass-2 table without tiling; the phase-stability comparison below does not apply to that case.

A p-th order explicit integrator accumulates a local truncation error of $O(h^{p+1})$ per step, giving a global phase error of $O(h^p)$ per period, growing to

$$\varepsilon_{\text{phase}}(T_{\text{final}}) = O(h^p T_{\text{final}}) \tag{31}$$

over the full integration. Symplectic integrators conserve a shadow Hamiltonian exactly, suppressing secular energy growth, but the shadow Hamiltonian differs from the true one by $O(h^p)$, giving a period error of $O(h^p)$ per cycle and accumulated phase error of $O(h^p T_{\text{final}})$—identical in scaling to RK4 [10].

GQM bounds drift via two contributions that must be accounted for separately. The first is the quadrature error: the half-period τ is computed once by adaptive Gauss–Kronrod quadrature [9] to absolute precision $\varepsilon_\tau \approx 10^{-13}$–$10^{-15}$, and exact half-period tiling then contributes a phase error of at most $N\varepsilon_\tau$ after N periods. The second is the Pass-3 inversion error: $s(t)$ is recovered by interpolation on the precomputed Pass-2 table $\{t_i, s_i\}$, and the interpolation error $\varepsilon_{\text{interp}}$ depends on the table resolution δt and the chosen scheme. For a cubic-spline interpolant on a uniform table with spacing δt, the inversion error is $O(\delta t^4)$ per query, independent of N. The total pipeline phase error at N periods is therefore bounded by

$$\varepsilon_{\text{phase}}^{\text{GQM}} \leq N\varepsilon_\tau + \varepsilon_{\text{interp}}(\delta t), \tag{32}$$

where the second term does not grow with N. In the numerical experiments of Table 4, a cubic-spline table with $\delta t = 10^{-4}$ s was used. For the $L = 1\,\text{m}$ pendulum ($T_{\max} = 1000\,\text{s}$, period $\tau \approx 2.20\,\text{s}$, $N \approx 454$ periods), this gives $\varepsilon_{\text{interp}} \approx 10^{-14}$ and a tiling contribution $N\varepsilon_\tau \approx 454 \times 10^{-15} \approx 5 \times 10^{-13}$—many orders of magnitude below both RK4 and symplectic integrators, with the interpolation error non-accumulating across periods. To illustrate the scaling advantage at larger horizons: for a hypothetical run of $N = 10^6$ periods with $\varepsilon_\tau \approx 10^{-15}$, the bound gives $N\varepsilon_\tau \approx 10^{-9}$, still far below ODE-integrator drift of $O(h^p T_{\text{final}})$. This bound is applicable to arbitrary planar curves for which no competing phase-stable method exists.

6.7 Limitations

The present formulation assumes:

1. a planar (2D) curve;
2. a particle (point mass), though the rolling extension admits rigid bodies with a single rolling degree of freedom;
3. gravity as the primary potential force (the rotating-frame kernel extends this to centrifugal potential, and any conservative force can be accommodated by replacing the gravitational kernel $\mathcal{K}$ as described in Section 3).

Extension to space curves (3D) requires the full Darboux frame and is deferred to future work.

7 Conclusion

The Geometric Quadrature Method (GQM) reformulates constrained particle dynamics on arbitrary planar curves as a three-pass spatial pipeline, delivering capabilities unavail-

able from standard ODE-based methods.

Pass 1 yields the speed field and normal contact force in exact closed form for any curve with an analytic height function—no quadrature, no approximation. This is the core structural advantage: the entire rail loading map, including force sign transitions and liftoff conditions, is accessible algebraically. **Pass 2** confines the irreducibly non-elementary time-of-flight computation to a single adaptive quadrature, evaluated to machine precision. **Pass 3** recovers phase-stable long-time trajectories for conservative (periodic) systems by exact half-period tiling, bounding phase error at $N\varepsilon_\tau$ independently of T_{final}; for dissipative kernels the motion is non-periodic and Pass 3 reduces to direct table inversion without tiling.

A central element enabling the method's extensibility is the **speed-field kernel** $\mathcal{A}(s)$, which encodes the physical force model in a modular, plug-and-play form. The kernel specifies how each arc-length element contributes to the total speed change—in exact analogy with the convolution kernel of the discrete piecewise-linear limit (Section 2.1). Six kernels are derived covering frictionless sliding, rolling with inertia, Coulomb friction, quadratic drag, surface tension, and rotating frames. A complementary dimensional reduction table (Table 3) reduces eight standard curve families—Cartesian graphs, circles, ellipses, parabolas, logarithmic spirals, catenaries, cycloids, and implicit curves—to this single framework by providing the arc-length element and curvature for each geometry. Importantly, **any conservative force field can be accommodated**: replacing the gravitational term in $\mathcal{A}$ with $-\nabla U \cdot \hat{\boldsymbol{t}}$ for an arbitrary potential $U(x, z)$ yields the generalized Pass-1 result $V^2(s) = V_0^2 + 2[U_0 - U(s)]$, with Pass 2 and Pass 3 proceeding unchanged.

The method's position is clear. For the simple pendulum, the phase-stability benchmark shows that GQM reduces accumulated phase and energy drift by many orders of magnitude compared with all standard time-stepping schemes—explicit and symplectic alike—over long simulations (see equation (32) and Table 4). For every other smooth planar curve—ellipses, spirals, catenaries, cycloids, cubic profiles, and arbitrary numerically defined tracks—Liouville's theorem [11] guarantees that no closed-form trajectory exists. In this vast, practically relevant regime, GQM is the unique approach providing both exact spatial quantities and phase-stable trajectories.

The cubic track example further demonstrates a geometric robustness advantage unique to GQM: the use of an algebraically signed normal and a continuously signed curvature eliminates the frame-flip artefacts that conventional Frenet-frame solvers produce at inflection points. This makes GQM directly applicable to realistic engineering tracks that combine convex and concave segments.

Practical applications include rail loading prediction, long-time phase-stable simulation of non-circular oscillators, parametric sweeps over curve families in design optimization, and any setting where exact spatial force maps are needed without full trajectory integration. The kernel substitution principle of Section 3 opens further domains: replacing the gravitational term with a central-force gradient $-(\mu/r^2)\,\mathrm{d}r/\mathrm{d}s$ recovers the vis-viva equation in Pass 1 and the Kepler time-of-flight integral in Pass 2, extending naturally to perturbed non-Keplerian orbits. For geometries that evolve slowly relative to the particle's oscillation frequency—vibrating rails, flexible beams—the kernel can be updated quasi-statically each period, preserving Pass-1 exactness in the adiabatic regime.

Future work will extend the framework to 3D space curves via the Darboux frame, and to impact and rebound modeling.

A Curvature Formulas for Standard Parametrizations

Cartesian graph $z = \varphi(x)$:

$$\kappa = \frac{\varphi''}{(1+\varphi'^2)^{3/2}}. \tag{33}$$

Parametric curve $\boldsymbol{r}(\lambda) = (x(\lambda), z(\lambda))$:

$$\kappa = \frac{\dot{x}\ddot{z} - \dot{z}\ddot{x}}{(\dot{x}^2 + \dot{z}^2)^{3/2}}, \tag{34}$$

where dots denote $\mathrm{d}/\mathrm{d}\lambda$.
Polar curve $r = f(\theta)$:

$$\kappa = \frac{f^2 + 2f'^2 - f\,f''}{(f^2 + f'^2)^{3/2}}. \tag{35}$$

Implicit curve $F(x, z) = 0$:

$$\kappa = \frac{F_{xx}F_z^2 - 2F_{xz}F_xF_z + F_{zz}F_x^2}{|\nabla F|^3}. \tag{36}$$

Statements and Declarations

Funding. The author declares that no funds, grants, or other support were received during the preparation of this manuscript.
Competing Interests. The author has no relevant financial or non-financial interests to disclose.
Data Availability. The Python script `GQM_Plots.py` used to generate all numerical results and figures is provided as supplementary material. No other datasets were generated or analysed during the current study.

References

[1] Bernoulli, J.: Problema novum ad cujus solutionem mathematici invitantur. Acta Eruditorum **1696**, 269 (1696)

[2] Goldstein, H., Poole, C., Safko, J.: Classical Mechanics, 3rd edn. Addison-Wesley, San Francisco (2002). ISBN: 978-0-201-65702-9

[3] Lagrange, J.L.: Mécanique Analytique. Desaint, Paris (1788)

[4] Shabana, A.A.: Frenet oscillations and Frenet–Euler angles: curvature singularity and motion-trajectory analysis. Nonlinear Dyn. **106**(1), 1–19 (2021). doi:10.1007/s11071-021-06798-1

[5] Bettamin, D., Shabana, A.A., Bosso, N., Zampieri, N.: Frenet force analysis in performance evaluation of railroad vehicle systems. Acta Mech. **232**(10), 4235–4259 (2021). doi:10.1007/s00707-021-03045-x

[6] Marques, F., Flores, P., Pimenta Claro, J.C., Lankarani, H.M.: A survey and comparison of several friction force models for dynamic analysis of multibody mechanical systems. Nonlinear Dyn. **86**(3), 1407–1443 (2016). doi:10.1007/s11071-016-2999-3

[7] Battin, R.H.: An Introduction to the Mathematics and Methods of Astrodynamics, rev. edn. AIAA Education Series. AIAA, Reston (1999). doi:10.2514/4.861543

[8] Prussing, J.E., Conway, B.A.: Orbital Mechanics. Oxford University Press, New York (1993). ISBN: 978-0-19-507834-3

[9] Piessens, R., de Doncker-Kapenga, E., Überhuber, C.W., Kahaner, D.K.: QUADPACK: A Subroutine Package for Automatic Integration. Springer, Berlin (1983). doi:10.1007/978-3-642-61786-7

[10] Leimkuhler, B., Reich, S.: Simulating Hamiltonian Dynamics. Cambridge Monographs on Applied and Computational Mathematics, vol. 14. Cambridge University Press, Cambridge (2004). doi:10.1017/CBO9780511614118

[11] Ritt, J.F.: Integration in Finite Terms: Liouville's Theory of Elementary Methods. Columbia University Press, New York (1948). doi:10.7312/ritt91596

[12] Šalinić, S.: Contribution to the brachistochrone problem with Coulomb friction. Acta Mech. **208**(1–2), 97–115 (2009). doi:10.1007/s00707-008-0134-3

[13] Šalinić, S., Obradović, A., Mitrović, Z., Rusov, S.: Brachistochrone with limited reaction of constraint in an arbitrary force field. Nonlinear Dyn. **69**(1–2), 211–222 (2012). doi:10.1007/s11071-011-0258-1

[14] Cherkasov, O.Yu., Malykh, E.V., Smirnova, N.V.: Brachistochrone problem and two-dimensional Goddard problem. Nonlinear Dyn. **111**(1), 243–254 (2023). doi:10.1007/s11071-022-07857-x

[15] Hairer, E., Lubich, C., Wanner, G.: Geometric Numerical Integration: Structure-Preserving Algorithms for Ordinary Differential Equations, 2nd edn. Springer Series in Computational Mathematics, vol. 31. Springer, Berlin (2006). doi:10.1007/3-540-30666-8